



CHORUS

This is the accepted manuscript made available via CHORUS. The article has been published as:

Resonant translational, breathing, and twisting modes of transverse magnetic domain walls pinned at notches

Peter J. Metaxas, Maximilian Albert, Steven Lequeux, Vincent Cros, Julie Grollier, Paolo Bortolotti, Abdelmadjid Anane, and Hans Fangohr

Phys. Rev. B **93**, 054414 — Published 12 February 2016

DOI: [10.1103/PhysRevB.93.054414](https://doi.org/10.1103/PhysRevB.93.054414)

Resonant translational, breathing and twisting modes of transverse magnetic domain walls pinned at notches

Peter J. Metaxas,^{1,2,*} Maximilian Albert,³ Steven Lequeux,² Vincent Cros,²
Julie Grollier,² Paolo Bortolotti,² Abdelmadjid Anane,² and Hans Fangohr³

¹*School of Physics, M013, University of Western Australia,
35 Stirling Hwy, Crawley WA 6009, Australia.*

²*Unité Mixte de Physique, CNRS, Thales, Univ. Paris-Sud,
Université Paris-Saclay, 91191, Palaiseau, France.*

³*Engineering and the Environment,
University of Southampton, Southampton, United Kingdom.*

Abstract

We study resonant translational, breathing and twisting modes of transverse magnetic domain walls pinned at notches in ferromagnetic nanostrips. We demonstrate that a mode's sensitivity to notches depends strongly on the mode's characteristics. For example, the frequencies of modes that involve lateral motion of the wall are the most sensitive to changes in the notch intrusion depth, especially at the narrow, more strongly confined end of the domain wall. In contrast, the breathing mode, whose dynamics are concentrated away from the notches is relatively insensitive to changes in the notches' sizes. We also demonstrate a sharp drop in the translational mode's frequency towards zero when approaching depinning which is confirmed, using a harmonic oscillator model, to be consistent with a reduction in the local slope of the notch-induced confining potential at its edge.

PACS numbers: 75.60.Ch, 75.78.Fg, 76.50.+g

I. INTRODUCTION

Domain walls (DWs) are (typically nano-scale) transition regions which separate oppositely oriented magnetic domains in ferromagnetic materials. Many promising future applications of DWs rely on the current-driven displacement or resonant excitation of DWs in ferromagnetic nanostrips, the latter representing a type of DW conduit. The range of DW applications is broad and includes spintronic memristors which use DW displacements to control device resistances^{1,2}, next generation logic³ and data storage⁴ devices (the latter often relying on DW-based shift registers⁵) and even devices for the capture and transport of magnetic microbeads with envisioned use in biotechnology^{6,7}. Resonant DW excitations⁸ refer to resonant precessional magnetization dynamics localized at a DW⁸⁻²¹. These excitations have been shown to have the potential to be exploited in numerous areas of device-focused research, including the design of radiofrequency electronic oscillators²², enabling control over spin wave propagation in magnonic devices^{23,24} and assisting with DW motion²⁵⁻²⁹ and DW depinning^{11,12,30-32}, the latter via resonant excitation of a DW within a pinning (or ‘trapping’) potential.

The ability to exploit resonant phenomena in applications will however rely on successful control of the resonant modes of DWs. It is known that large geometrical constrictions such as notches (also widely used for positional control^{5,33-36}) in micron-scale strips can be used to tune the frequency of a DW’s translational mode²². For smaller³⁷ device geometries however, uniform fabrication of small notches may become challenging since the notches’ dimensions will likely become comparable to those characteristic of edge roughness or lithographic defects.

In this work we show how different DW resonances have different sensitivities to notches and that these sensitivities can be linked to the nature of the mode and the structure of the DW. For example, modes which involve either local or global translation of the wall can be highly sensitive to the presence, size and position of the notch. Our work focuses in particular on the resonant properties of pinned head-to-head transverse domain walls [TDWs, Fig. 1(a)] which arise in thin, narrow, in-plane magnetized strips³⁸. Here, the TDWs are pinned at triangular notches located on the edges of the strip. We use a numerical eigenmode method to study three TDW resonances, corresponding to translational^{10,11,22,39}, twisting^{16,40} and breathing^{10,41-45} excitations of the TDW. The latter mode has recently

been studied for oscillator applications⁴⁶ and we demonstrate that this mode has the lowest sensitivity to changes in notch depths, making it an appealing choice when fabricating devices with robust resonant frequencies. The eigenmode method we use also enables the study of the translational mode in the vicinity of the static depinning field where we find a sharp drop off in this mode’s frequency. This dramatic change in frequency can be linked directly to the position-dependence of the slope of the notch-induced confining potential which, as done in experiment^{13,47}, we probe by field-induced displacements of the TDW within the potential.

II. MICROMAGNETIC SIMULATION METHOD

Many numerical studies of resonant modes in confined geometries use time domain (‘ring-down’) methods in which Fourier analysis of precessional magnetization dynamics is employed to extract resonant mode frequencies and spatial profiles. These methods require the system to be subjected to an external excitation^{16,40,48–50}, often a pulsed magnetic field. In contrast, eigenmode methods^{51,52} enable a direct calculation of resonant magnetic modes from a system’s equilibrium magnetic configuration, $\mathbf{m}_0(\mathbf{r})$ (as do dynamical matrix methods⁵³). This enables the observation of the full mode spectrum without requiring careful choice of the ringdown excitation’s symmetry. It also enables us to study DW modes at fields which are in the close neighborhood of the static depinning field where excited translational resonances could otherwise resonantly depin^{11,12,30–32} the wall.

Our simulations were run on a Permalloy strip having saturation magnetization $M_S = 860$ kA/m and exchange stiffness $A_{\text{ex}} = 13$ pJ/m. The strip has tapered ends and two central notches for TDW pinning [Fig. 1(a)]. Unless otherwise noted, the notches are located at $x = 0$, the strip thickness is 5 nm and the total length is 750 nm. Simulations were run using the finite element micromagnetic package, Finmag, which is the successor to Nmag⁵⁴ and is based on a similar design.

Magnetic eigenmodes are determined from $\mathbf{m}_0(\mathbf{r})$ with Finmag using a method similar to that described by d’Aquino *et. al.*⁵¹ It is valid for small time-dependent oscillations, $\mathbf{dm}(\mathbf{r}, t)$, around $\mathbf{m}_0(\mathbf{r})$ and has been used recently to model ferromagnetic resonances in magnonic crystals⁵⁵. The basic principle is to linearize the (undamped) LLG equation around the equilibrium state $\mathbf{m}_0(\mathbf{r})$, resulting in a linear system of ordinary differential equations

(ODEs) for the oscillations $\mathbf{dm}(\mathbf{r}, t)$ which has the form $\frac{\partial}{\partial t}\mathbf{dm}(\mathbf{r}, t) = A \cdot \mathbf{dm}(\mathbf{r}, t)$ with a matrix $A \in \mathbb{R}^{3N \times 3N}$, where N is the number of nodes in the finite element mesh⁵⁶. This system of ODEs has a full set of solutions of the form $\mathbf{dm}(\mathbf{r}, t) = e^{i2\pi ft}\mathbf{v}(\mathbf{r})$. Each solution vector $\mathbf{v} \in \mathbb{C}^{3N}$ represents an eigenmode of the nanostrip corresponding to the frequency f ; its complex coefficients encode the local amplitudes and relative phases of the eigenmode at the mesh nodes. In theory, the eigenfrequencies f are purely real. However, due to the formulation of the problem as a non-Hermitian eigenvalue problem the eigensolver returns complex solutions with a small imaginary component due to numerical inaccuracies. We quote the real parts of f . Eigenmodes localized at the TDW can be identified by visual inspection of the spatially resolved eigenvectors. Either the dynamic component, $\mathbf{dm}(\mathbf{r}, t)$, may be inspected alone or it can be scaled and added to $\mathbf{m}_0(\mathbf{r})$, enabling a visualization of the actual TDW dynamics for each mode (e.g. see mode animations⁵⁷).

To find $\mathbf{m}_0(\mathbf{r})$, the system was initialized with a trial head-to-head TDW configuration centered on $x = 0$ and allowed to relax with damping parameter $\alpha = 1$, typically until $dm/dt < 1^\circ/\text{ns}$ at all points in the strip. For a strip width of 75 nm and a thickness of 5 nm, using the stricter criterion $dm/dt < 0.1^\circ/\text{ns}$ resulted in changes in the mode frequencies of 1.1 Mhz or less ($\leq 0.04\%$). The relaxed configuration was a pinned TDW for all studied geometries³⁸. Note that the TDW [Fig. 1(a)] is wider at the $+y$ side of the strip which will be important for determining TDW-notch interactions.

We used a non-uniform finite element meshing with a characteristic internode length of $l_{\text{mesh}} = 3$ nm at $x = 0$ (less than the NiFe exchange length⁵⁸ of 5.7 nm). There was a smooth transition to $l_{\text{mesh}} = 8$ nm at the ends of the strip. This reduces computational time and memory use. However, a post-relaxation mesh coarsening⁵⁵ could potentially be applied to future studies. We note that except for those simulations in which magnetic fields close to the DW depinning field are applied, the error in the mode frequency associated with the non-uniform meshing was less than 1%. However, as a result of the non-uniform mesh, we present results only on those modes which are localized on the TDW near the center of the strip since modes associated with the domains themselves will be in regions with l_{mesh} close to or larger than the exchange length. This said, such modes (typically multiple GHz) can also be excited in experiment together with the DW modes²¹.

III. TDW MODES

The three lowest frequency TDW modes correspond to translational, breathing or twisting deformations. In Figs. 1(b-d) these three calculated modes are shown (as a snapshot of the mode's dynamic component, $\mathbf{dm}(\mathbf{r}, t)$ at a time such that $\mathbf{dm}(\mathbf{r}, t)$ is large) for a 75 nm strip with symmetric, triangular notches, each with width, $w_{\text{notch}} = 20$ nm and a depth of intrusion into the strip, $d_{\text{notch}} = 10$ nm. The translational mode (2.70 GHz) corresponds to an oscillatory, side-to-side motion of the TDW away from the notches [Fig. 1(b)]. For the breathing mode^{10,40-45} [6.57 GHz, Fig. 1(c)], dynamics are concentrated at the edges of the domain wall with the excitations mirrored around $x = 0$. The dynamics of this mode result in an oscillatory change in the TDW's width as a function of time. For this strip width, the highest frequency mode is the 7.03 GHz twisting mode [Fig. 1(d)]. This mode involves the TDW's two ends (near the top/bottom of the strip) moving laterally but in opposite directions. Idealizing the TDW as a string crossing the nanostrip, this mode has similarities to a standing wave with a zero-displacement node ($\mathbf{dm} \approx 0$) near $y = 0$. As shown below, and in contrast to what is observed for the translational mode, a finite frequency for the breathing and twisting modes is non-reliant on confinement (i.e. they are intrinsic $f > 0$ TDW excitations). Indeed, Wang *et al.*⁴⁰ have observed what appear to be similar breathing and twisting modes for unpinned TDWs.

We now confirm that the frequencies of the translational and breathing modes obtained using the eigenmode method have good consistency with those obtained via a time domain ringdown method. To do this, we applied external excitation fields to the system which had the correct symmetry to couple to each of these two modes (we note however that we were not able to efficiently excite the twisting mode either with uniform or non-uniform excitations⁵⁹). For the translational mode, we applied an excitation field in the x direction: x -fields will displace the wall and thus can be used to couple to the translational mode. For the breathing mode, we applied a field in the y direction which acts to increase the TDW width, thus coupling to the breathing mode's width oscillation. Fourier analysis of the resultant ringdown dynamics ($m_x(t)$ for f_{trans} and $m_y(t)$ for f_{breathe}) at a strip width of 80 nm demonstrated successful field-induced excitation of the translational and breathing modes at $f_{\text{trans}} = 2.6 \pm 0.1$ GHz and $f_{\text{breathe}} = 6.4 \pm 0.1$ GHz. These frequencies are in good agreement with the eigenmode results of $f_{\text{trans}} = 2.61$ GHz and $f_{\text{breathe}} = 6.38$ GHz

for $w = 80$ nm [as per Fig. 5 which will be discussed later with regards to strip-width dependence of the mode frequencies].

Although this work does not attempt to address spin torque driven auto-oscillations associated with the TDW modes, radiofrequency magnetic fields (or effective fields associated with spin torques) having symmetries as discussed above can be used experimentally to drive the breathing and translational modes. This could be achieved using x or y oriented (real or effective) magnetic fields generated by striplines¹⁸ (x or y), Oersted fields due to in-plane current injection⁶⁰ (y) or tailorable⁶¹ Slonczewski or field-like spin torques (x or y) under perpendicular current injection in magnetic tunnel junctions (MTJs)^{21,62-64} and all-metallic magnetoresistive stacks⁶⁵. Indeed, Lequeux *et al*²¹ recently observed the translational mode under microwave frequency current injection in a MTJ. Numerous other studies have also demonstrated the excitation of the translational mode using spin torques due to in-plane current injection^{8,11,22} and new possibilities exist with regards to the use of spin-orbit torques⁶⁶⁻⁶⁸.

A. Notch dependence

We now examine the dependence of the modes on the size of the notches used to pin the TDW. The translational and twisting modes both involve some movement of the TDW away from the energetically favorable $x = 0$ position. This can either be a global side-to-side movement of the TDW (as for the translational mode) or a local side-to-side movement (as for the twisting mode where out of phase lateral TDW movements arise at opposite edges of the strip). Lateral movement has strong implications for notch sensitivity: both the twisting and translational modes have a strong dependence on the notch size. In contrast, dynamics of the breathing mode are concentrated at the lateral edges of the TDW structure (and thus away from the central notches) which results in a much weaker sensitivity to the notch and changes to it.

To demonstrate the different sensitivities of each mode to notch size, we have plotted each TDW eigenfrequency in Figs. 2(a,b) as a function of the notches' intrusion depths for a 75 nm wide strip with a 20 nm ($= w_{\text{notch}}$) wide notch. Here, both notches have the same geometry on the two sides of the strip. One will notice immediately that the twisting and translational modes (i.e. those with a translational nature) are highly dependent on

d_{notch} . The translational mode's frequency, f_{trans} , decreases smoothly with d_{notch} , going to zero at $d_{\text{notch}} = 0$ [Fig. 2(a)]. This latter result is consistent with the wall being free to translate laterally at $f_{\text{trans}} = 0$ in the absence of pinning (i.e. $d_{\text{notch}} = 0$ corresponds to a smooth-edged strip with no notches). The twisting mode frequency, f_{twist} , also depends quite strongly on d_{notch} , reducing by $\sim 40\%$ (~ 2 GHz) when changing d_{notch} from 20 nm to 0 nm [Fig. 2(b)]. In contrast, the breathing mode frequency, f_{breathe} , changes by only 1.5% over the same range of d_{notch} values [Fig. 2(b)]. Note also in Fig. 2(b) that f_{breathe} and f_{twist} remain finite at $d_{\text{notch}} = 0$, consistent with these modes being intrinsic TDW excitations for which the observation of a finite eigenfrequency is non-reliant on notch-induced, lateral TDW confinement.

Despite both notches being geometrically identical, one can see from the mode snapshots in Figs. 1(b,d) that both the twisting and translational modes' dynamics are largest at the wide end of the TDW. This suggests that this end of the TDW has a weaker lateral confinement than the narrow end of the TDW. This is confirmed in Fig. 3 which shows a TDW being pushed away from the notches under the action of a magnetic field, H , applied along the x axis ($H < H_{\text{depin}}$, the static depinning field). It is indeed the less strongly pinned wide end of the TDW which is displaced furthest from the notch. To see what effect notches at each end of the wall have on the modes, we show in Figs. 2(c,d) results obtained while varying d_{notch} on only one side of the strip (either at the wide end or at the narrow end of the TDW) while keeping the other notch's intrusion depth fixed at 10 nm. We indeed find that f_{trans} is most sensitive to changes of d_{notch} at the narrow end of the wall, that notch being dominant in determining f_{trans} (and in generating pinning). For example, reducing d_{notch} from 10 nm to 2 nm at the narrow end of the wall [filled circles in Fig. 2(c)] generates a very strong, 40% reduction in f_{trans} . This reduction in f_{trans} is accompanied by a transition to a more pure translation of the TDW structure in its entirety rather than an excitation in which the highest amplitude dynamics occur at the wide end of the TDW [as in Fig. 1(a)]. This occurs since both ends of the wall now experience a relatively weak pinning. If we change d_{notch} only at the wide end of the wall however, we observe much weaker changes in f_{trans} [crossed open circles in Fig. 2(c)] with similar trends seen for f_{twist} . The d_{notch} -dependence of f_{breathe} again remains very weak.

To test the limits of the d_{notch} -insensitivity of f_{breathe} , simulations were run with the notch at the wide end of the wall displaced away from $x = 0$ for the 75 nm wide strip. This did

lead to small changes in f_{breathe} ($d_{\text{notch}} = 10$ nm, $w_{\text{notch}} = 20$ nm) with some distortion of the breathing mode observed when the notch was right at the edge of the TDW. However the maximum frequency change still remained within 3% of the value observed for two laterally centered notches. We also looked at the percentage variation of f_{breathe} for two other strip widths for centrally located notches (60 nm and 100 nm wide strips again having a 5 nm thickness). We found the lowest sensitivity occurred for larger strip widths where the notch intrudes comparatively less far into the strip and thus presumably generates the weakest change to the energy landscape that is experienced by the TDW (confirmed in Sec. III C for the translational mode). Reducing the thickness of the layer also led to a further reduced sensitivity. This can be seen in Fig. 4(b) where we again plot resonance data for 60 nm and 75 nm wide strips but this time with a reduced (2.5 nm) strip thickness. An important point to note from Fig. 4 is that the breathing mode remains highly insensitive to changes in the d_{notch} of small notches for all studied strip widths. Indeed, we see the largest changes in f_{breathe} when d_{notch} becomes larger than about 12 nm suggesting that small defects should have only a very minor effect on the breathing mode. In contrast, the other two modes exhibit the highest sensitivity to changes in the notch intrusion depth when that depth is already small (Fig. 2).

We briefly note that changes in the *width* of the notch (for a fixed notch depth of 10 nm) yielded only weak changes for f_{breathe} and f_{twist} . Over a range of notch widths from 5 nm to 50 nm we observed $\Delta f_{\text{twist}} \leq 3$ % and $\Delta f_{\text{breathe}} \leq 2$ %. The change in f_{trans} was also quite small when reducing the notch width below 20 nm ($\Delta f_{\text{trans}} \leq 6$ %). However, broadening the notch to 50 nm led to a strong reduction in f_{trans} of > 60 %, presumably due to a strongly reduced confinement by the broader notches (the effect of confinement on f_{trans} is discussed further below).

B. Strip width dependence

When holding the notch geometry constant ($w_{\text{notch}} = 20$ nm and $d_{\text{notch}} = 10$ nm), an increasing the strip width generates an reduction in each of the TDW mode frequencies [Fig. 5(a)]. The breathing and twisting modes remain highest in frequency and their similar frequencies, coupled with slightly different width dependencies, results in a mode crossing which occurs at $w = w_c \approx 88.4$ nm for this 5 nm thick strip [Figs. 5(b)]. At $w \approx w_c$,

a translational mode as well as two other distinct TDW modes are found with the latter appearing as ‘hybrid’ twisting-breathing modes [e.g. Fig. 5(c)]. However, their hybrid nature is due to the arbitrary basis chosen by the eigensolver: each hybrid mode can in fact be shown to be a linear combination of the ‘pure’ orthogonal twisting and breathing eigenmodes (see Appendix A). Indeed, we expect no coupling between different modes due to the exclusion of damping and non-linear terms in our approach⁵¹. The hybrid nature of the modes remains clearly identifiable via visual inspection for $|w - w_c| \lesssim 1.5$ nm. However, as $|w - w_c|$ increases, the computed modes become more ‘pure’ (i.e. a dominant breathing or twisting characteristic). In Fig. 5(b), all modes at $w \neq 88.4$ nm are labeled either as twisting or breathing with the label corresponding to the mode which is dominant. Analogous hybrid modes were also calculated for a similar geometry using the mode solver in the SpinFlow3D simulation package. Some details on this solver have been given previously⁵².

C. Width dependent confinement and its effect on the translational mode

We now turn specifically to the width dependence of the translational mode which will be shown to be linked to the width-dependence of the notch-induced confinement of the TDW. Note that some qualitative models for the higher frequency breathing and twisting mode frequencies as a function of strip width are given in Appendix B.

The frequency of the translational mode of the pinned TDW, f_{trans} , as a function of $H < H_{\text{depin}}$ is shown for a number of strip widths in Fig. 6 (again we use $w_{\text{notch}} = 20$ nm and $d_{\text{notch}} = 10$ nm). Note that for fields above the depinning field (i.e. $H > H_{\text{depin}}$), the system’s relaxed configuration is that of a quasi-uniformly magnetized strip with the TDW having been displaced towards the end of the strip and annihilated during the simulation’s relaxation stage (i.e. the moment where we first determine $\mathbf{m}_0(\mathbf{r})$). As such, there is no TDW mode data above H_{depin} (since no TDW is present). For all strip widths, f_{trans} shows a weak negative monotonic dependence on H for small H/H_{depin} . However, f_{trans} drops sharply to zero (i.e. again going toward the case of a free TDW) as $H \rightarrow H_{\text{depin}}$. DW resonant frequency *reductions* near depinning have been previously observed experimentally^{13,47}. Note that for $H \approx H_{\text{depin}}$, f_{trans} exhibits a stronger sensitivity to the relaxation parameters of the simulation, requiring the use of a smaller dm/dt near H_{depin} . f_{trans} as well as the determined value of H_{depin} itself is also more sensitive to the non-uniform meshing than the undeformed

TDW at $H = 0$. For example, a slightly higher H_{depin} ($< 1\%$ relative change) was found when using $l_{\text{mesh}} = 3$ nm throughout the structure at $w = 60$ nm revealing some influence on the f versus H plot from the non-uniform meshing. This influence is highest for the strongly deformed walls near H_{depin} where f_{trans} varies quickly with H .

As H_{depin} is approached, f_{twist} also drops in frequency [Fig. 6(b)] which may, in part, be due to the wide part of the TDW being away from the upper notch (as per Fig. 3). This shifts the wall-concentrated dynamics at the upper edge of the strip away from the notch [Fig. 6(c)]. We have already seen that strongly reducing the size of the upper notch for an undisplaced wall reduces f_{twist} [Fig. 2(d)] and the case of the displaced wall is somewhat analogous as the upper part of the wall is now far from the notch (i.e. we effectively have $d_{\text{notch}} \rightarrow 0$ at the location of the upper end of the TDW). Unlike f_{trans} , f_{twist} remains finite near depinning, analogous to the finite f_{twist} observed for $d_{\text{notch}} = 0$ in Fig. 2(b). The breathing mode again shows a very weak change in its frequency even near depinning where the spatial profile of the mode is strongly deformed [Fig. 6(d)] with respect to the case of a non-displaced wall [Fig. 1(c)]. Once again this highlights the robustness of f_{breathe} (to notch geometry and now in-plane-field-induced deformation).

In Fig. 6 an increased f_{trans} can be observed at small strip widths (a trend which has already been seen in Fig. 5(a)) and this is accompanied by an increased H_{depin} . To understand this, we will take the previously used approach of modeling a parabolic, notch-induced TDW confining potential^{12,22,31,69,70}. This results in a spring like behavior of the DW with a restoring force of $-k_N x$ where k_N is the pinned TDW's spring constant and x its displacement from the center of the strip. The equilibrium position of the TDW at a given H is determined by a balance between this restoring force and the effective force due to the applied magnetic field^{31,70}. This force can be estimated from the x -derivative of the change in Zeeman energy for the displaced TDW: $2\mu_0 w t M_S H$ where $t = 5$ nm is the strip thickness and $\mu_0 = 4\pi \times 10^{-7}$ H/m. Note that we neglect the locally altered strip width at the notch.

To extract k_N , in Fig. 7(a) we plot the equilibrium position for the domain wall versus H for the data shown in Fig. 6. The position of the field-deformed TDW (see, e.g., Fig. 3), x , was determined from the spatially averaged x -component of the magnetization along the strip^{31,70}. For low field, there is good linearity between x and H , indicative of a close-to-parabolic pinning potential. At larger fields however, there is a faster than linear growth in the x_{TDW} , the effect of which will be discussed further below. From the data in the linear

region (which has slope $dx/dH = g_{\text{linear}}$), we can estimate a value for k_N :

$$k_N = (2\mu_0 wt M_S)(x/H)^{-1} = (2\mu_0 wt M_S)g_{\text{linear}}^{-1} \quad (1)$$

which, plotted in Fig. 7(b) versus the strip width, reduces with increasing strip width. At small widths, this results in a stiffer domain wall (there, the notch, which has a fixed size here, makes a larger *relative* intrusion into the strip).

We can now use the values of k_N to estimate f_{trans} at $H = 0$ and compare to the data in Fig. 5^{31,70}:

$$f_{\text{trans}} = \frac{1}{2\pi} \sqrt{\frac{k_N}{m_w}}. \quad (2)$$

Here, m_w is the mass (e.g.^{8,39,71}) of the TDW. Note that an increased resonant frequency is observed for smaller widths [Fig. 6] where k_N is higher [Fig. 7(b)]. Thus we can immediately see that our results are qualitatively consistent with the trend suggested by Eq. (2), at least under the assumption of a w -independent mass. To obtain numerical values for f_{trans} however, we must estimate the mass for which we use the damping-free ($\alpha = 0$) expression^{31,70} (a similar expression is given by Krüger⁷²):

$$m_w = \frac{2\mu_0 wt}{\gamma^2(N_z - N_y)\Delta}. \quad (3)$$

$\gamma = 2.210713 \times 10^5$ m/A.s and $\Delta = \Delta_T$ is the Thiele DW width⁷³ [field dependent, as per Fig. 7(c)] which is defined by $2/\Delta_T = 1/(wt) \int_V (dm/dx)^2$ where V is the nanostrip volume. N_y and N_z are the demagnetizing factors for the TDW in the y and z directions. To calculate these factors, we used expressions given by Aharoni⁷⁴, treating the TDW as a uniformly magnetized slab with a length in the y direction equal to the strip width, a height in the z direction equal to the strip thickness and a width in the x direction of $\rho\Delta_T(H = 0)$. ρ , a scaling factor, is the only free parameter since the strip width and strip thickness are fixed. It sets the width of the rectangular prism used for the demagnetizing field calculation as a fraction of the Thiele width.

As can be seen in Fig. 7(d), good agreement between the eigenmode simulation at $H = 0$ and the spring model [Eq. (2)] is found for the four studied thicknesses when using $\rho = \frac{1}{3}$. This means that the slab used for the demagnetizing factor calculation is ~ 10 nm wide in the x direction, essentially covering a central narrow slice of the TDW structure where the

magnetization is quasi-uniformly magnetized in the y -direction [Fig. 8(a)] and thus close to our original model of a uniformly magnetized slab. Note that the magnetization undergoes an almost complete rotation from being aligned along $+x$ to $-x$ over a much larger distance $\sim \pi\Delta_T$ [Fig. 8(a)]. It is however the central region of the TDW which appears to be the relevant part in this approach.

The effective width of the pinning potential, L_{pin} , defined here as the maximum displacement of the TDW measured before depinning [Fig. 7(a)], increases with Δ_T [read from Fig. 8(b)] and thus with strip width. However, the depinning field (the field at which the wall can escape from the pinning potential) is smallest in these wide strips [Fig. 6(a)]. Thus, although the pinning potential has a larger effective width when the strip width is high [increasing by a factor of ~ 1.4 , Fig. 7(c)], it appears to be the wide strips' reduced k_N [which changes more strongly with width, reducing by a factor of ~ 2 , Fig. 7(b)] which is dominant in determining the wide strips' reduced depinning fields (and reduced f_{trans}).

Finally, we address the faster than linear growth in the TDW position versus H [Fig. 7(a)] which is a result of the pinning potential having a reduced steepness near its edge⁴⁷. We can show that Eq. (2) remains valid in describing f_{trans} at $x \neq 0$ (i.e. even in the non-parabolic^{13,47} part of the potential) if we replace k_N by a local effective spring constant

$$k_{N,\text{eff}}(x(H)) = \frac{2\mu_0 wt M_S}{dx/dH}. \quad (4)$$

In Fig. 9 $\sqrt{(dx_{\text{TDW}}/dH)^{-1}}$ ($\propto f_{\text{trans}}$ as per Eq. (2)) has been plotted versus the simulated values of f_{trans} for all studied strips. We have neglected any field-induced change in the TDW mass ($m_w = m_w(H = 0)$) and have used a numerical derivative of the data in Fig. 7(a) to determine dx_{TDW}/dH . We find a high degree of linearity over the full field range for all strip widths. This confirms the continued validity of Eq. (2) and demonstrates that the sharp drop-off in f_{trans} near H_{depin} (Fig. 6) can be linked with a change in the local gradient of the pinning potential at its edge, the latter determining the resonant frequency of the displaced TDW in the small oscillation limit. Note that from Eq. (2), we expect that the slope of the data in Fig. 9 will be $2\pi\sqrt{m_w(H = 0)/2\mu_0 wt M_S}$. We have plotted the ratio of the predicted slope to the fitted slope in the inset of Fig. 9(d) where we indeed find consistency to within 2.5%.

IV. CONCLUSION

We have numerically calculated eigenmodes of transverse domain walls (TDWs) which are pinned at triangular notches in in-plane magnetized nanostrips. This enabled the study of translational, twisting and breathing resonances of TDWs and the effect that notch geometry and field-induced TDW displacements have on these modes.

The twisting and translational modes both involve either local or global lateral translation of the wall structure within the notch-induced pinning potential. This leads to a clear sensitivity to changes in the intrusion depth of the notches especially to that of the notch at the narrow end of the TDW structure which has a dominant role in laterally confining the TDW. The breathing mode, which is characterized by dynamics concentrated at the lateral edges of the TDW (and thus away from the notches), was relatively insensitive to changes in the notch intrusion depth and width. For example, when varying the notch intrusion depth from 0 to 20 nm, the largest change in the mode's frequency was 3% (observed for the narrowest studied strip width of 60 nm). Based on our results, this sensitivity may be able to be further reduced by using a thinner or wider strip.

These results may be relevant when choosing which TDW mode to exploit in DW oscillators or when aiming to individually or simultaneously excite (multiple) DWs pinned at different positions within a strip (e.g. in shift registers^{5,46,75}). This is because certain modes (i.e. those with a translational nature) will be more sensitive to non-uniformity of notch geometries and/or to the presence of small uncontrolled defects. Our results suggest that the breathing mode frequency will be the most robust to the introduction of small unwanted defects or non-uniformity in fabricated notch geometries, especially at larger strip widths or smaller notch depths. In contrast, having a translational or twisting mode frequency which is robust to small changes in the notch geometry appears to be reliant on having relatively large notches.

For a fixed notch geometry, the frequencies of all modes increased with decreasing strip width, making this an important device parameter to control. In the particular case of the translational mode's frequency, its width dependence could be reproduced with a spring model for notch-induced TDW confinement. Furthermore, the eigenmode method (which does *not* rely on the forced driving of the TDW's resonant dynamics) allowed us to determine the translational mode frequencies over a wide range of fields, including in the vicinity of

the static depinning field where the translational mode frequency dropped sharply towards zero as the TDW was displaced to the edge of the confining potential. At low applied magnetic fields (and thus low TDW displacements), the notch-induced confining potential was parabolic, enabling us to analytically reproduce the simulated translational mode frequency at zero field. At large fields (which generated larger displacements of the TDW within the confining potential), the growth of the pinning potential's energy with displacement was sub-parabolic (as seen previously for a vortex DW⁴⁷). Here the spring model could still be used to reproduce the translational mode frequencies as long as the local slope of the pinning potential was used to calculate the spring constant. These calculations required a DW mass determination with a good match between quasi-analytics and simulation achieved when using only the very narrow central part of the TDW for the calculation of the TDW's demagnetizing factors (critical for the determination of the TDW mass).

Finally, we note that f_{trans} is finite only in the presence of confinement. In contrast, f_{breathe} and f_{twist} remain large and finite even without a notch or close to the depinning field, demonstrating an intrinsic $f > 0$ characteristic, albeit with some (mode-dependent) sensitivity to the notches' presence.

ACKNOWLEDGMENTS

This research was supported by the Australian Research Council's Discovery Early Career Researcher Award funding scheme (DE120100155), an EPSRC Doctoral Training Centre grant (EP/G03690X/1), the French ANR grant ESPERADO (11-BS10-008) and the University of Western Australia's Research Collaboration Award and Early Career Researcher Fellowship Support. PJM also acknowledges support from the United States Air Force, Asian Office of Aerospace Research and Development (AOARD). The authors thank M. Kostylev, I.S. Maksymov, D. Chernyshenko, M. Beg, O. Hovorka, T. Valet and G. Albuquerque for useful discussions.

Appendix A: Extraction of pure modes from hybrid modes

To demonstrate that each 'hybrid' mode [Fig. 5(c)] is a linear combination of the 'pure' orthogonal twisting and breathing eigenmodes, we let $\mathbf{v}_1, \mathbf{v}_2$ be the hybrid mode eigenvectors

as returned by the solver (their complex entries encode the amplitude and relative phase of the magnetization oscillations at each mesh node). To show that these can be reduced to the ‘pure’ modes we need to find complex scalars a_1, a_2 such that the linear combination $\mathbf{v} = a_1\mathbf{v}_1 + a_2\mathbf{v}_2$ represents a breathing or twisting mode. The breathing mode is characterized by being fully symmetric about the y -axis, i.e. the oscillations in the left and right half of the nanostrip are out of phase by 180° : $\mathbf{v}(x, y, z) = -\mathbf{v}(-x, y, z)$. The expression $\int |\mathbf{v}(x, y, z) + \mathbf{v}(-x, y, z)|$ thus measures the deviation from symmetry for an eigenmode \mathbf{v} and we can find the ‘most symmetric’ linear combination by minimizing this with respect to a_1, a_2 . Since each eigenvector is only determined up to a scalar, we can assume that $a_1 = 1$ (or $a_2 = 1$), reducing the dimensionality of the optimization problem. The obtained linear combination is confirmed to be an eigenvector corresponding to a breathing mode. Similarly, the twisting mode can be recovered by using the condition $\mathbf{v}_{\text{twist}}(x, y, z) = \mathbf{v}_{\text{twist}}(-x, y, z)$.

Appendix B: Modeling the twisting and breathing modes

We detail here two simple qualitative models for the f_{breathe} and f_{twist} strip width dependencies seen in Fig. 5(a).

The general trend of decreasing f_{twist} with w for fixed notch geometry is qualitatively consistent with a string-like mode that is confined across the strip having a single node in the strip’s center (i.e. with wavelength $\sim 2w$ and thus a frequency $\propto \frac{1}{w}$). We plot f_{twist} versus $\frac{1}{w}$ in Fig. 10(a) with reasonable linearity at larger widths.

Liu and Grütter have constructed a model for DW width resonances in magnetic films⁴² which predicts that f_{breathe} will be proportional to $\sqrt{K_{\text{eff}}}$ where K_{eff} is the effective anisotropy energy associated with the domain wall. For our static TDW (here in a confined geometry rather than a continuous layer), K_{eff} comes from the TDW’s demagnetizing energy and can be written as $\frac{1}{2}\mu_0 M_S^2 N_y$ (e.g.⁷⁶), giving $f_{\text{breathe}} \propto \sqrt{N_y}$. Indeed, this relation reproduces the observed f_{breathe} trend relatively well over the entire strip width range, as calculated for a number of strip width values in Fig. 10. To determine N_y , we used the same slab approach as used in Sec. III B.

* peter.metaxas@uwa.edu.au

- ¹ X. Wang, Y. Chen, H. Xi, H. Li, and D. Dimitrov, *IEEE Elec. Dev. Lett.* **30**, 294 (2009).
- ² N. Locatelli, V. Cros, and J. Grollier, *Nat. Mater.* **13**, 11 (2013).
- ³ J. A. Currivan-Incorvia, S. Siddiqui, S. Dutta, E. R. Evarts, J. Zhang, D. Bono, C. A. Ross, and M. A. Baldo, *Nat. Comms.* **7**, 10275 (2016).
- ⁴ S. Fukami, T. Suzuki, K. Nagahara, N. Ohshima, Y. Ozaki, S. Saito, R. Nebashi, N. Sakimura, H. Honjo, K. Mori, C. Igarashi, S. Miura, N. Ishiwata, and T. Sugibayashi, in *VLSI Technology, 2009 Symposium on* (2009) p. 230.
- ⁵ S. S. P. Parkin, M. Hayashi, and L. Thomas, *Science* **320**, 190 (2008).
- ⁶ M. Donolato, P. Vavassori, M. Gobbi, M. Deryabina, M. F. Hansen, V. Metlushko, B. Ilic, M. Cantoni, D. Petti, S. Brivio, and et al., *Adv. Mater.* **22**, 2706 (2010).
- ⁷ E. Rapoport, D. Montana, and G. S. D. Beach, *Lab Chip* **12**, 4433 (2012).
- ⁸ E. Saitoh, H. Miyajima, T. Yamaoka, and G. Tatara, *Nature* **432**, 203 (2004).
- ⁹ J. Winter, *Physical Review* **124**, 452 (1961).
- ¹⁰ A. Rebei and O. Mryasov, *Phys. Rev. B* **74**, 014412 (2006).
- ¹¹ D. Bedau, M. Kläui, S. Krzyk, U. Rüdiger, G. Faini, and L. Vila, *Phys. Rev. Lett.* **99**, 146601 (2007).
- ¹² L. Thomas, M. Hayashi, X. Jiang, R. Moriya, C. Rettner, and S. Parkin, *Science* **315**, 1553 (2007).
- ¹³ R. Moriya, L. Thomas, M. Hayashi, Y. B. Bazaliy, C. Rettner, and S. S. P. Parkin, *Nat Phys* **4**, 368372 (2008).
- ¹⁴ C. W. Sandweg, S. J. Hermsdoerfer, H. Schultheiss, R. Schäfer, B. Leven, and B. Hillebrands, *J. Phys. D: Appl. Phys.* **41**, 164008 (2008).
- ¹⁵ L. Bocklage, B. Krüger, P. Fischer, and G. Meier, *Phys. Rev. B* **81**, 054404 (2010).
- ¹⁶ P. E. Roy, T. Trypiniotis, and C. H. W. Barnes, *Phys. Rev. B* **82**, 134411 (2010).
- ¹⁷ L. O'Brien, E. R. Lewis, A. Fernández-Pacheco, D. Petit, R. P. Cowburn, J. Sampaio, and D. E. Read, *Phys. Rev. Lett.* **108**, 187202 (2012).
- ¹⁸ L. Bocklage, S. Motl-Ziegler, J. Topp, T. Matsuyama, and G. Meier, *J. Phys.: Condens. Matter* **26**, 266003 (2014).
- ¹⁹ A. T. Galkiewicz, L. O'Brien, P. S. Keatley, R. P. Cowburn, and P. A. Crowell, *Phys. Rev. B* **90** (2014).
- ²⁰ S. Sangiao and M. Viret, *Phys. Rev. B* **89**, 104412 (2014).

- ²¹ S. Lequeux, J. Sampaio, P. Bortolotti, T. Devolder, R. Matsumoto, K. Yakushiji, H. Kubota, A. Fukushima, S. Yuasa, K. Nishimura, Y. Nagamine, K. Tsunekawa, V. Cros, and J. Grollier, *Appl. Phys. Lett.* **107**, 182404 (2015).
- ²² S. Lepadatu, O. Wesseley, A. Vanhaverbeke, R. Allenspach, A. Potenza, H. Marchetto, T. R. Charlton, S. Langridge, S. S. Dhesi, and C. H. Marrows, *Phys. Rev. B* **81**, 060402(R) (2010).
- ²³ C. Bayer, H. Schultheiss, B. Hillebrands, and R. L. Stamps, *IEEE Trans. Mag.* **41**, 3094 (2005).
- ²⁴ S. J. Hermsdoerfer, H. Schultheiss, C. Rausch, S. Schafer, B. Leven, S.-K. Kim, and B. Hillebrands, *Appl. Phys. Lett.* **94**, 223510 (2009).
- ²⁵ Y. Le Maho, J.-V. Kim, and G. Tatara, *Phys. Rev. B* **79**, 174404 (2009).
- ²⁶ D. S. Han, S. K. Kim, J. Y. Lee, S. J. Hermsdoerfer, H. Schultheiss, B. Leven, and B. Hillebrands, *Appl. Phys. Lett.* **94**, 112502 (2009).
- ²⁷ M. Jamali, H. Yang, and K. J. Lee, *Appl. Phys. Lett.* **96**, 242501 (2010).
- ²⁸ A. Janutka, *IEEE Mag. Lett.* **4**, 4000104 (2013).
- ²⁹ X. G. Wang, G. H. Guo, Y. Z. Nie, D. W. Wang, Z. M. Zeng, Z. X. Li, and W. Tang, *Phys. Rev. B* **89**, 144418 (2014).
- ³⁰ T. Nozaki, H. Maekawa, M. Mizuguchi, M. Shiraishi, T. S. and Y. Suzuki, H. Maehara, S. Kasai, and T. Ono, *Appl. Phys. Lett.* **91**, 082502 (2007).
- ³¹ E. Martinez, L. Lopez-Dias, O. Alejos, and L. Torres, *Phys. Rev. B* **77**, 144417 (2008).
- ³² P. J. Metaxas, A. Anane, V. Cros, J. Grollier, C. Deranlot, A. Lemaître, S. Xavier, C. Ulysse, G. Faini, F. Petroff, and A. Fert, *Appl. Phys. Lett.* **97**, 182506 (2010).
- ³³ M. Hayashi, L. Thomas, C. Rettner, R. Moriya, X. Jiang, and S. S. P. Parkin, *Phys. Rev. Lett.* **97** (2006).
- ³⁴ D. Petit, A. V. Jausovec, D. Read, and R. P. Cowburn, *J. Appl. Phys.* **103**, 114307 (2008).
- ³⁵ L. Bogart, D. Atkinson, K. O'Shea, D. McGrouther, and S. McVitie, *Phys. Rev. B* **79**, 054414 (2009).
- ³⁶ A. Kunz and J. D. Priem, *IEEE Trans. Mag.* **46**, 1559 (2010).
- ³⁷ J. A. Currivan, S. Siddiqui, S. Ahn, L. Tryputen, G. S. D. Beach, M. A. Baldo, and C. A. Ross, *J. Vac. Sci. Technol. B* **32**, 021601 (2014).
- ³⁸ Y. Nakatani, A. Thiaville, and J. Miltat, *J. Magn. Magn. Mater.* **290**, 750 (2005).
- ³⁹ J. Rhensius, L. Heyne, D. Backes, S. Krzyk, L. J. Heyderman, L. Joly, F. Nolting, and M. Klaui, *Physical Review Letters* **104**, 067201 (2010).

- ⁴⁰ X.-G. Wang, G.-H. Guo, J. A. C.-F. Bland, Y.-Z. Nie, Q.-L. Xia, and Z.-X. Li, *Journal of Magnetism and Magnetic Materials* **332**, 56 (2013).
- ⁴¹ R. L. Stamps, A. S. Carriço, and P. E. Wigen, *Phys. Rev. Lett.* **55**, 6473 (1997).
- ⁴² Y. Liu and P. Grütter, *J. Appl. Phys.* **83**, 5922 (1998).
- ⁴³ A. L. Dantas, M. S. Vasconcelos, and A. S. Carriço, *J. Magn. Magn. Mater* **226**, 1604 (2001).
- ⁴⁴ K. Matsushita, M. Sasaki, J. Sato, and H. Imamura, *J. Phys. Soc. Jpn* **81**, 043801 (2012).
- ⁴⁵ M. Mori, W. Koshibae, S. Hikino, and S. Maekawa, *J. Phys.: Condens. Matter* **26**, 255702 (2014).
- ⁴⁶ K. Matsushita, M. Sasaki, and T. Chawanya, *J. Phys. Soc. Jpn.* **83**, 013801 (2014).
- ⁴⁷ D. Bedau, M. Kläui, , M. T. Hua, S. Krzyk, U. Rüdiger, GFaini, and L. Vila, *Phys. Rev. Lett.* **101**, 256602 (2008).
- ⁴⁸ M. Grimsditch, G. K. Leaf, H. G. Kaper, D. A. Karpeev, and R. E. Camley, *Phys. Rev. B* **69**, 174428 (2004).
- ⁴⁹ R. D. McMichael and M. D. Stiles, *J. Appl. Phys* **97**, 10J901 (2005).
- ⁵⁰ M. Dvornik, P. V. Bondarenko, B. A. Ivanov, and V. V. Kruglyak, *J. Appl. Phys.* **109**, 07B912 (2011).
- ⁵¹ M. d’Aquino, C. Serpico, G. Miano, and C. Forestiere, *J. Comp. Phys.* **228**, 6130 (2009).
- ⁵² V. V. Naletov, G. de Loubens, G. Albuquerque, S. Borlenghi, V. Cros, G. Faini, J. Grollier, H. Hurdequint, N. Locatelli, B. Pigeau, A. N. Slavin, V. S. Tiberkevich, C. Ulysse, T. Valet, and O. Klein, *Phys. Rev. B* **84**, 224423 (2011).
- ⁵³ R. Zivieri and G. Consolo, *Adv. Cond. Matt. Phys.* **2012**, 1 (2012).
- ⁵⁴ T. Fischbacher, M. Franchin, G. Bordignon, and H. Fangohr, *IEEE Trans. Mag.* **43**, 2896 (2007).
- ⁵⁵ P. J. Metaxas, M. Sushruth, R. Begley, J. Ding, R. C. Woodward, I. Maksymov, M. Albert, W. Wang, H. Fangohr, A. Adeyeye, and M. Kostylev, *Appl. Phys. Lett.* **106**, 232406 (2015).
- ⁵⁶ The matrix A has the form $A = \gamma \cdot \Lambda(\mathbf{m}_0) \cdot (H_0 - \mathbf{H}'_{\text{eff}}(\mathbf{m}_0))$, where γ is the gyromagnetic ratio, $\Lambda(\mathbf{m}_0)$ is a block-diagonal matrix representing the point-wise cross product with \mathbf{m}_0 at each mesh node (i.e., it is defined such that $\Lambda(\mathbf{m}_0) \cdot \mathbf{w} = \mathbf{m}_0 \times \mathbf{w}$ holds for any $\mathbf{w} \in \mathbb{R}^{3N}$), and H_0 is a block-diagonal matrix where each block is a 3×3 identity matrix multiplied by the dot product $\mathbf{H}_{\text{eff}} \cdot \mathbf{m}_0$ evaluated at the mesh node corresponding to this block. The matrix A can be derived by starting from the undamped LLG equation $\frac{\partial \mathbf{m}}{\partial t} = -\gamma \cdot \mathbf{m} \times \mathbf{H}_{\text{eff}}$, making the ansatz

$\mathbf{m}(\mathbf{r}, t) = \mathbf{m}_0 + \mathbf{d}\mathbf{m}(\mathbf{r}, t)$, multiplying out the cross product, neglecting any higher-order terms and applying suitable rearrangements to the equation in order to isolate $\mathbf{d}\mathbf{m}(\mathbf{r}, t)$. See Eq. (95) in Ref. 51.

- ⁵⁷ See supplemental material at [URL will be inserted by AIP] for animated .GIF files which show the full resonant TDW dynamics, $\mathbf{m}_0(\mathbf{r}) + \mathbf{d}\mathbf{m}(\mathbf{r}, t)$, for each of the three TDW modes at a strip width of 75 nm with $d_{\text{notch}} = 10$ nm and $w_{\text{notch}} = 20$ nm.
- ⁵⁸ G. S. Abo, Y.-K. Hong, J.-H. Park, J.-J. Lee, W. Lee, and B.-C. Choi, *IEEE Trans. Mag.* **49**, 4937 (2013).
- ⁵⁹ To do this, we attempted both spatially uniform excitations along the x , y and diagonal axes and a non-uniform excitation, the latter having a field parallel to the x -axis everywhere but with a strength proportional to the y -position; i.e. pointing in positive (negative) x -direction at positive (negative) y as per Fig. 1(a).
- ⁶⁰ V. Uhler, S. Pizzini, N. Rougemaille, V. Cros, E. Jimenez, L. Ranno, O. Fruchart, M. Urbanek, G. Gaudin, J. Camarero, C. Tieg, F. Sirotti, E. Wagner, and J. Vogel, *Phys. Rev. B* **83**, 020406R (2011).
- ⁶¹ A. Khvalkovskiy, K. A. Zvezdin, Y. V. Gorbunov, V. Cros, J. Grollier, A. Fert, and A. K. Zvezdin, *Phys. Rev. Lett.* **102**, 067206 (2009).
- ⁶² A. Chanthbouala, R. Matsumoto, J. Grollier, V. Cros, A. Anane, A. Fert, A. V. Khvalkovskiy, K. A. Zvezdin, N. Nishimura, Y. Nagamine, H. Maehara, K. Tsunekawa, A. Fukushima, and S. Yuasa, *Nat. Phys.* **7**, 626 (2011).
- ⁶³ P. J. Metaxas, J. Sampaio, A. Chanthbouala, R. Matsumoto, A. Anane, A. K. Zvezdin, K. Yakushiji, H. Kubota, A. Fukushima, S. Yuasa, K. Nishimura, Y. Nagamine, H. Maehara, K. Tsunekawa, V. Cros, and J. Grollier, *Sci. Rep.* **3**, 1829 (2013).
- ⁶⁴ J. Sampaio, S. Lequeux, P. J. Metaxas, A. Chanthbouala, R. Matsumoto, K. Yakushiji, H. Kubota, A. Fukushima, S. Yuasa, K. Nishimura, and et al., *Applied Physics Letters* **103**, 242415 (2013).
- ⁶⁵ C. T. Boone, J. A. Katine, M. Carey, J. R. Childress, X. Cheng, and I. Krivorotov, *Phys. Rev. Lett.* **104**, 097203 (2010).
- ⁶⁶ A. V. Khvalkovskiy, V. Cros, D. Apalkov, V. Nikitin, M. Krounbi, K. A. Zvezdin, A. Anane, J. Grollier, and A. Fert, *Physical Review B* **87** (2013).
- ⁶⁷ K.-S. Ryu, L. Thomas, S.-H. Yang, and S. Parkin, *Nat. Nanotechnol.* **8**, 527533 (2013).

- ⁶⁸ S. Emori, U. Bauer, S.-M. Ahn, E. Martinez, and G. S. D. Beach, *Nat Mater* **12**, 611616 (2013).
- ⁶⁹ L. Thomas, M. Hayashi, X. Jiang, R. Moriya, C. Rettner, and S. S. P. Parkin, *Nature* **443**, 197 (2006).
- ⁷⁰ E. Martinez, L. Lopez-Diaz, O. Alejos, L. Torres, and C. Tristan, *Phys. Rev. Lett.* **98**, 267202 (2007).
- ⁷¹ G. Tatara and H. Kohno, *Physical Review Letters* **92**, 086601 (2004).
- ⁷² B. Krüger, *Current-Driven Magnetization Dynamics: Analytical Modeling and Numerical Simulation*, Ph.D. thesis, Universität Hamburg (2011).
- ⁷³ A. Thiaville, Y. Nakatani, F. Pichon, J. Miltat, and T. Ono, *Eur. Phys. J. B* **60**, 1527 (2007).
- ⁷⁴ A. Aharoni, *J. Appl. Phys.* **83**, 3432 (1998).
- ⁷⁵ J.-S. Kim, M.-A. Mawass, A. Bisig, B. Krüger, R. M. Reeve, T. Schulz, F. Büttner, J. Yoon, C.-Y. You, M. Weigand, and et al., *Nat. Commun.* **5**, 1 (2014).
- ⁷⁶ M. T. Bryan, S. Bance, J. Dean, T. Schrefl, and D. A. Allwood, *J. Phys.: Condens. Matter* **24**, 024205 (2012).

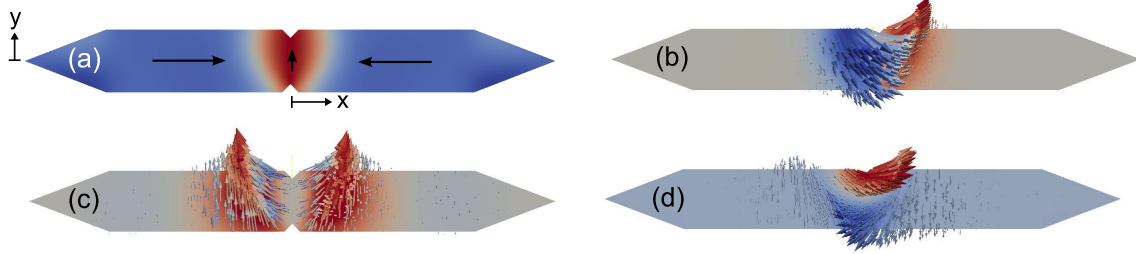


FIG. 1. (Color online) (a) Zero-field equilibrium magnetization configuration, $\mathbf{m}_0(\mathbf{r})$, in a 75 nm wide NiFe strip with symmetric notches ($w_{\text{notch}} = 20$ nm, $d_{\text{notch}} = 10$ nm) containing a head-to-head TDW with m_y color scaling. The black arrows indicate the local magnetization direction. The x and y axis origins are also shown. (b-d) Snapshots of the translational, breathing and twisting modes showing the dynamic component only ($\mathbf{dm}(\mathbf{r})$). The translational mode snapshot (b) uses m_y color scaling and is taken when the TDW is displaced to the right ($+x$) at which point there is a significant dynamic $+m_x$ component. The breathing mode snapshot (c) also uses m_y color scaling and is taken at the point during the TDW width oscillation when the width is larger than its equilibrium value. There is thus a large dynamic $+m_y$ component at the TDW edges which broadens the TDW. The twisting mode snapshot (d) uses m_x color scaling and is taken at the point when the wide end of the TDW ($+y$) is displaced to the right and the narrow end of the TDW ($-y$) is displaced to the left. See also animations of the modes⁵⁶.

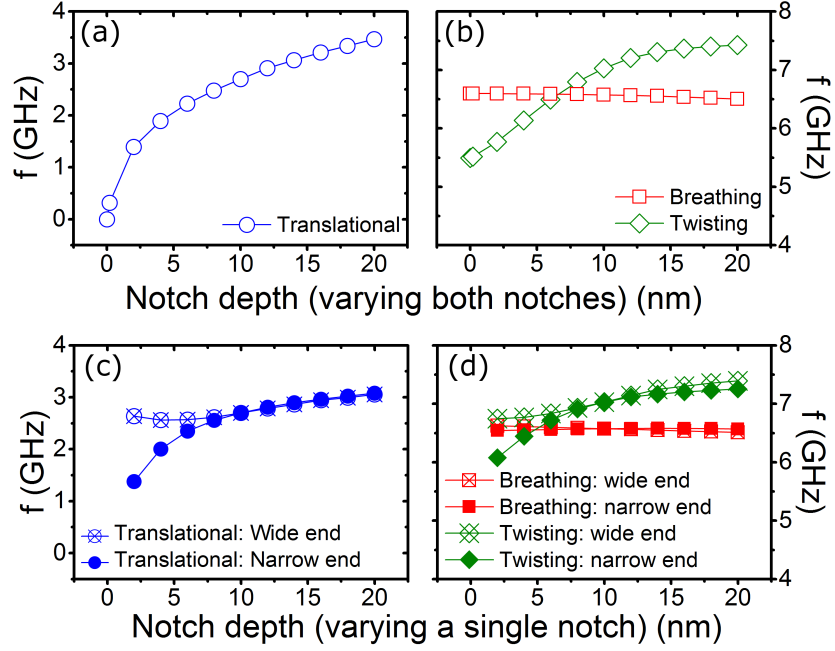


FIG. 2. (Color online) (a,b) TDW eigenfrequencies versus d_{notch} when varying d_{notch} for both notches simultaneously. (c,d) Eigenfrequencies when varying d_{notch} only at one side of the strip, either at the wide end or narrow end of the wall while keeping the other notch with $d_{\text{notch}} = 10$ nm. For all data $w_{\text{notch}} = 20$.



FIG. 3. (Color online) Deformed domain wall in a 75 nm strip for $H_x = 5530$ A/m.

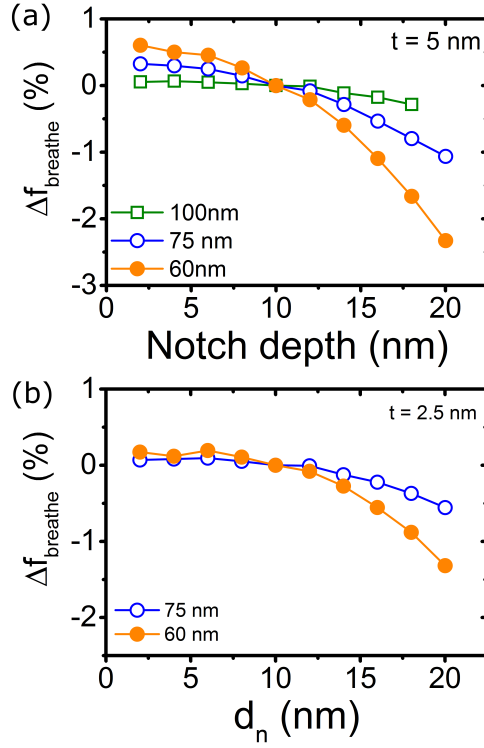


FIG. 4. (Color online) Percentage change in f_{breathe} with respect to f_{breathe} at $d_{\text{notch}} = 10$ plotted against d_{notch} for (a) 5 nm thick strips and (b) 2.5 nm thick strips at various strip widths (see legends).

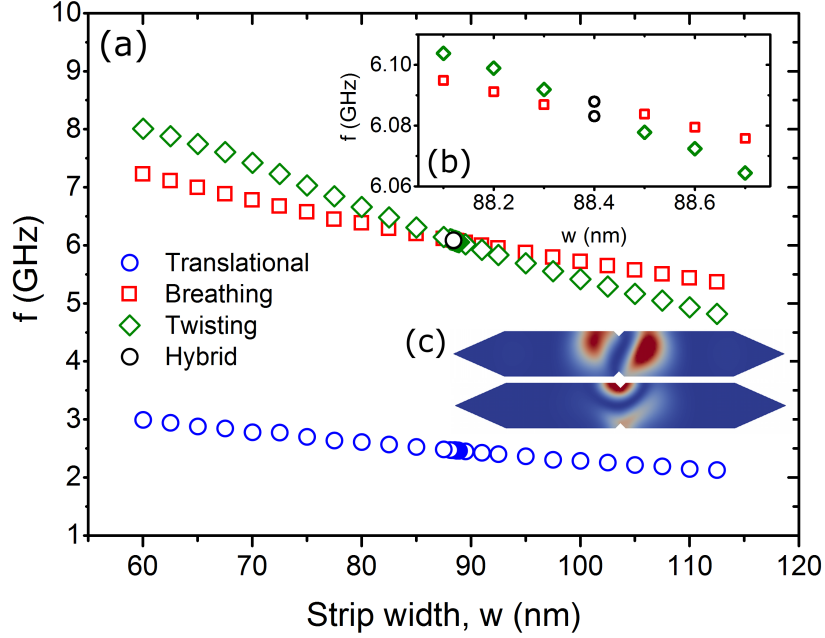


FIG. 5. (Color online) (a) Frequencies of the three TDW eigenmodes as a function of strip width, w . The notches are symmetric ($d_{\text{notch}} = 10$ nm, $w_{\text{notch}} = 20$ nm). At $w = 88.4$ nm the calculated modes are ‘hybrid’ breathing-twisting modes (see inset, b). (c) shows snapshots of the amplitude of the dynamic component (red) of the hybrid modes found for $w = 88.2$ nm at 6.091 GHz (upper, primarily a breathing mode) and 6.099 GHz (lower, primarily a twisting mode).

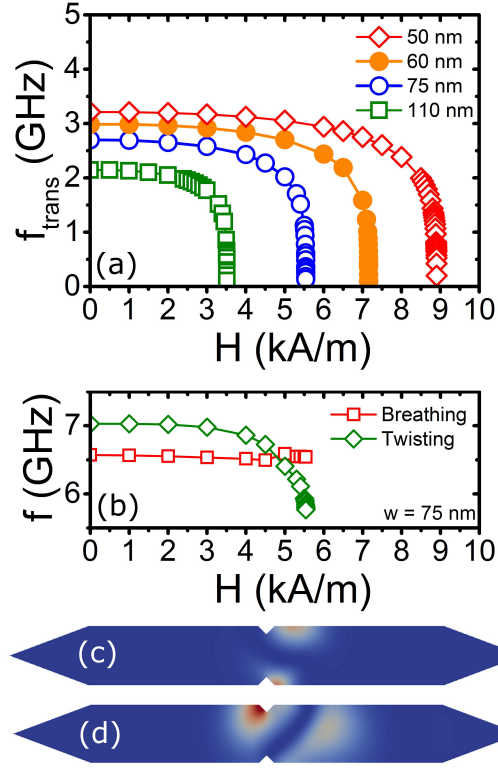


FIG. 6. (Color online) (a) f_{trans} versus in-plane field, H (oriented along $+x$), for strip widths of 50, 60, 75 and 110 nm ($d_{\text{notch}} = 10$ nm and $w_{\text{notch}} = 20$ nm). (b) f_{breath} and f_{twist} versus H at a strip width of 75 nm. (c,d) Snapshots of the amplitude of the dynamic component (red) of the magnetization for the (c) twisting and (d) breathing modes at a strip width of 75 nm for $H = 5530$ A/m (i.e. close to depinning).

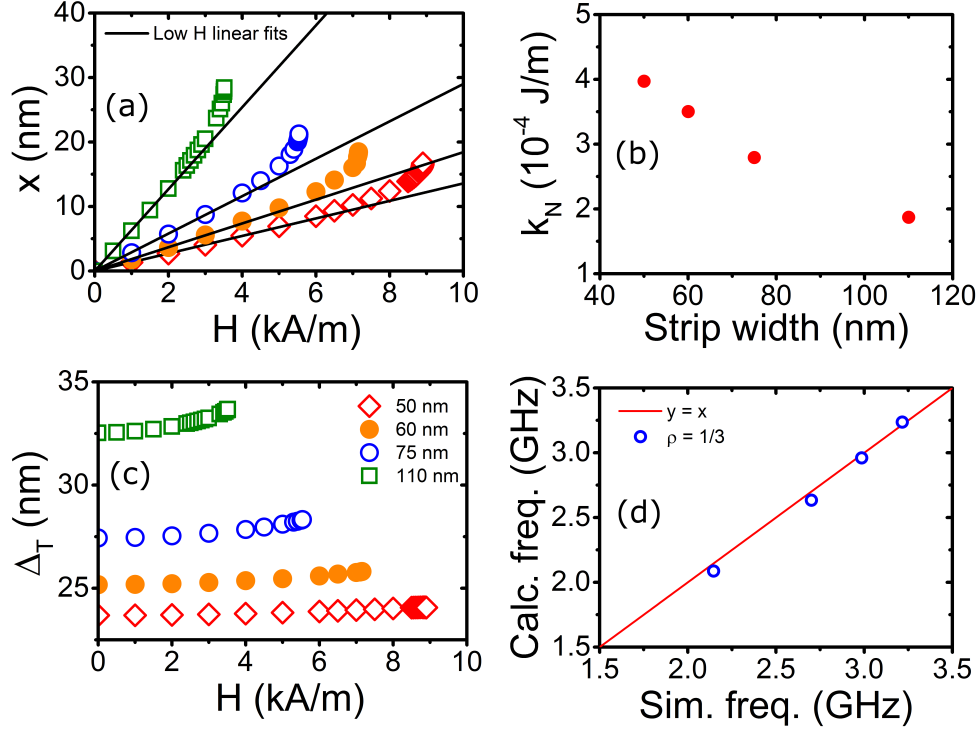


FIG. 7. (Color online) (a) Equilibrium TDW position versus H applied along the $+x$ direction. Solid lines are linear fits to the low field data (typically the first 4-5 points). (b) TDW spring constant versus strip width calculated from the linear fits in (a) using Eq. (1). (c) Thiele domain wall width of the H -deformed TDWs versus H . (d) Calculated f_{trans} (calculated as per the text using the data in (a,c) and Eqs. (1-3)) versus the simulated f_{trans} [Fig. 6(a)].

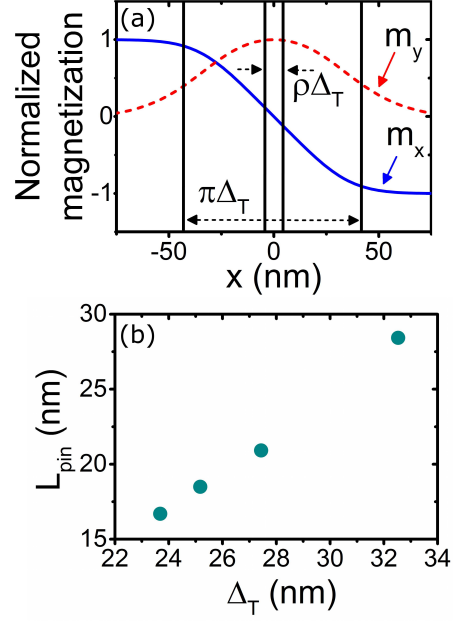


FIG. 8. (Color online) (a) x -dependence of the x and y components of the magnetization taken at $y = 0$ (at the center of the strip). Δ_T is the Thiele DW width and ρ is a scaling factor used in the demagnetizing field calculation. (b) Effective width of the pinning potential (L_{pin}) estimated from the maximum displacement of the TDW before depinning (taken from Fig. 7(a)) plotted against Δ_T for strip widths of 50, 60, 75 and 110 nm. The largest width strip has the largest Δ_T .

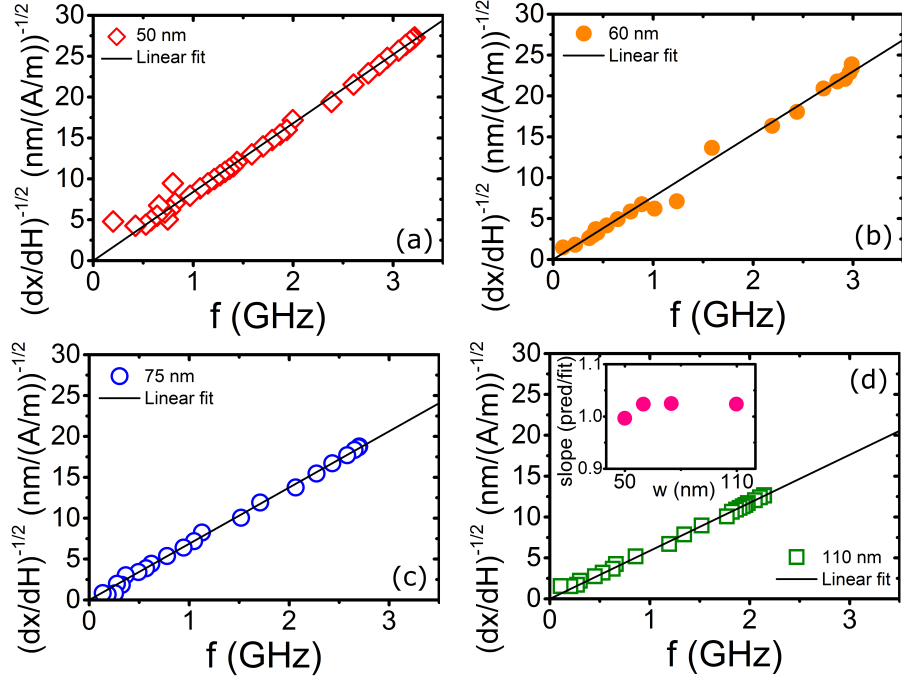


FIG. 9. (Color online) Plot of $(dx_{\text{TDW}}/dH)^{-1}$, proportional to the local effective spring constant, versus f_{trans} for field-displaced TDWs in strip widths of (a) 50, (b) 60, (c) 75, and (d) 110 nm. $(dx_{\text{TDW}}/dH)^{-1}$ and f_{trans} data were taken, respectively, from Figs. 7(a) and 6. Solid lines are linear fits to the data assuming a zero x-axis intercept. The inset in (d) shows the ratio of the slope of the data in (a-c) predicted from the spring model to the measured slope.

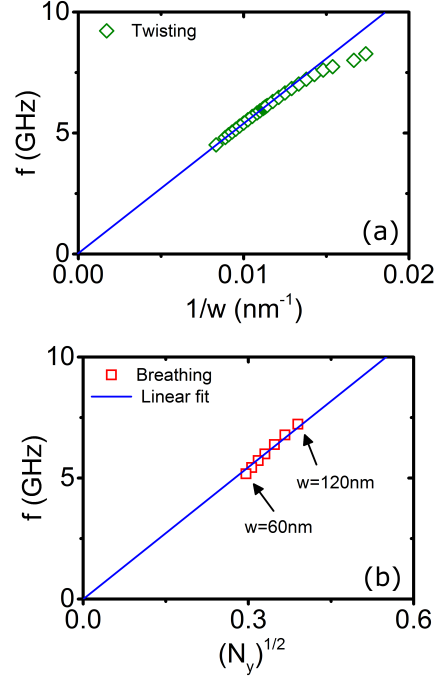


FIG. 10. (Color online) (a) f_{twist} versus the inverse strip width. (b) f_{breath} versus $\sqrt{N_y}$ (see text for N_y calculation) for a number of strip widths. The linear fits have been obtained by constraining the x-axis intercept to zero.